JGR Oceans

RESEARCH ARTICLE
10.1029/2025JC022929

Impact of Intertidal Areas on Tidal Propagation in Tidally Dominated Estuaries. Part II: A Comprehensive Sensitivity Study

Renjie Zhu[1,2,3,4], **Wei Zhang**[1,2,3], **and Xiaoyan Wei**[4]

[1]State Key Laboratory of Water Disaster Prevention, Hohai University, Nanjing, China, [2]Key Laboratory of Ministry of Education for Coastal Disaster and Protection, Hohai University, Nanjing, China, [3]College of Harbour, Coastal and Offshore Engineering, Hohai University, Nanjing, China, [4]National Oceanography Centre, Liverpool, UK

Key Points:
- Intertidal areas amplify tides in deep, short, weakly frictional, strongly convergent estuaries, but damp tides under opposite conditions
- Intertidal flow velocities can reach 60% of channel flow in shallow estuaries with strong channel friction or weak intertidal friction
- Currents over intertidal areas reduce the channel-intertidal water exchange, offsetting up to 45% of overall effects of intertidal areas

Supporting Information:
Supporting Information may be found in the online version of this article.

Correspondence to:
X. Wei,
xwei@noc.ac.uk

Citation:
Zhu, R., Zhang, W., & Wei, X. (2026). Impact of intertidal areas on tidal propagation in tidally dominated estuaries. Part II: A comprehensive sensitivity study. *Journal of Geophysical Research: Oceans*, *131*, e2025JC022929. https://doi.org/10.1029/2025JC022929

Received 26 MAY 2025
Accepted 11 JAN 2026

Author Contributions:
Conceptualization: Renjie Zhu, Wei Zhang, Xiaoyan Wei
Formal analysis: Renjie Zhu, Xiaoyan Wei
Funding acquisition: Renjie Zhu, Wei Zhang, Xiaoyan Wei
Investigation: Renjie Zhu, Xiaoyan Wei
Methodology: Renjie Zhu, Xiaoyan Wei
Project administration: Wei Zhang, Xiaoyan Wei
Resources: Wei Zhang, Xiaoyan Wei
Software: Renjie Zhu
Supervision: Wei Zhang, Xiaoyan Wei
Validation: Xiaoyan Wei
Visualization: Renjie Zhu, Xiaoyan Wei
Writing – original draft: Renjie Zhu, Xiaoyan Wei

Abstract

This is Part II of a two-part theoretical study on the impact of intertidal areas on tides in tidally dominated estuaries. Part I developed an analytical model that resolves tidal motions in the channel and intertidal regions which are dynamically coupled through the water exchange between both regions. This model considers both effects of water storage (IWS) and longitudinal currents (ILC) over intertidal areas. Part II applies the model to a broad range of parameter space to systematically investigate how the strength of currents over intertidal areas and the significance of ILC effects on tides respond to changes in estuary characteristics and forcing conditions. Our results demonstrate intertidal areas amplify tides in systems with large channel depths, short lengths, weak friction in the channel, and strong width convergence, while causing tidal damping under contrary conditions. Model experiments show significant currents over intertidal areas in tidally dominated estuaries over a large range of parameter spaces, particularly under conditions of small channel depths, strong channel bed friction, and weak intertidal bed friction. These currents over intertidal areas reach up to 60% of channel flow velocities. The ILC-induced water exchange is almost out of phase with that induced by IWS. Therefore, the ILC effect reduces the total channel-intertidal water exchange and counterbalances up to 45% of the above-mentioned effects of intertidal areas on tides. This highlights the potential importance of currents over intertidal areas in shaping tidal dynamics in tidally dominated estuaries, emphasizing the need for improved monitoring and modeling of these processes.

Plain Language Summary

Intertidal zones, such as mudflats and saltmarshes, can influence how tides propagate in estuaries, but these effects are complex and not yet fully understood. This study builds on earlier work by applying a simplified mathematical model to explore how intertidal areas affect tides. We examined a wide range of estuary shapes, sizes, and conditions to understand what controls the strength of along-estuary currents over intertidal areas and their role in tidal changes. Our results show that intertidal areas can either amplify or weaken tides depending on factors like estuary depth, length, and bottom resistance. We found that strong currents over intertidal areas commonly develop in shallow, strongly frictional estuaries and can flow at speeds up to 60% of those in the main channel. These currents often counteract other effects of intertidal areas, reducing their overall impact by up to 45%. This means that currents over intertidal areas can play a key role in shaping tidal behavior and should be more carefully considered in efforts to observe, manage, and model estuarine systems.

1. Introduction

Estuarine intertidal areas are vital ecosystems with multiple benefits in reducing flooding risks by attenuating wave energy, improving water quality by filtering pollutants, providing habitats for marine species, and mitigating global warming by capturing and storing carbon (Möller et al., 2014). However, intertidal zones are rapidly shrinking under the pressure of climate change (e.g., extreme storms, sea-level rise) and anthropogenic interventions (e.g., land reclamation, dredging, damming), thereby escalating the risks of erosion, flooding, and biodiversity loss in estuaries (Murray et al., 2019). To restore the sustainable functioning of these estuarine ecosystems, intertidal habitats have increasingly been protected and created as nature-based solutions in many estuaries, for example, the Ems, Thames, Scheldt estuaries (C. Li et al., 2016; Restemeyer et al., 2019; Stark et al., 2017). Given the important role of tides in estuarine hazards, it is essential to understand how changes in

Writing – review & editing: Renjie Zhu, Wei Zhang, Xiaoyan Wei

intertidal areas affect tidal propagation, particularly under the varying estuary characteristics and forcing conditions posed by human activities and climate change.

Many numerical and analytical studies have been conducted to investigate the impact of intertidal areas (see Figure 1) on tidal propagation, as reviewed in Part I of this study. Zheng et al. (2003), C. Li et al. (2016), and Stark et al. (2017) found that the intertidal areas play an important role in dampening principal tidal oscillations in Satilla River, Ems, and Scheldt estuaries. In contrast, Oey et al. (2007), L. Li et al. (2012), and L. Li et al. (2018) reported that intertidal areas tend to enhance the principal tide in Cook Inlet, Darwin Harbor, and Xiangshan Bay. This highlights the importance of understanding the dominant processes that control the roles of intertidal zones in affecting tidal dynamics under various conditions. However, numerical simulations (e.g., L. Li et al., 2012; Oey et al., 2007; Zheng et al., 2003) are computationally expensive with various physical processes integrated into the model, thereby not ideal for understanding the contributions of different physical processes to the effects of intertidal areas on tides and their sensitivities to a large range of parameter spaces. Analytical models (e.g., Friedrichs & Madsen, 1992; Jay, 1991; Winterwerp & Wang, 2013) are particularly effective in revealing the underlying mechanisms by which intertidal areas influence estuarine tidal propagation and how the effects of intertidal areas depend on various estuary and forcing characteristics. However, existing analytical studies only account for the water storage effects of intertidal areas by assuming zero flow velocity over intertidal areas, that is, full momentum sink.

This assumption may be reasonable for micro- or meso-tidal estuaries with narrow intertidal areas, such as the Delaware estuary (with the ratio of intertidal width to channel width $r_B \sim 0$, see Friedrichs & Aubrey, 1994) and the Columbia estuary ($r_B \sim 0.1$, Giese & Jay, 1989) in the US, and the Ems estuary ($r_B \sim 0.1$, Winterwerp et al., 2013) and the Elbe estuary ($r_B \sim 0.1$, Dronkers, 2016) in Germany. In these estuaries, the water depth and longitudinal velocity in the intertidal area are significantly smaller than those in the channel. Hence, the effect of along-estuary currents over intertidal areas is negligible in these systems, as considered in previous studies (e.g., Jay, 1991). In macrotidal estuaries or tidal inlets, however, intertidal zones can be extensive and even wider than the channel. Among these systems are the Ribble estuary ($r_B \sim 1.5$, van der Wal et al., 2002) and the Humber estuary ($r_B \sim 0.5$, Townend & Whitehead, 2003) in the UK, the Seine estuary ($r_B \sim 1$, Cundy et al., 2007) in France, and the Gomso Bay ($r_B \sim 2$, Kim & Cho, 2017) in Korea. Considerable tidal velocities were observed over intertidal areas of these systems, with velocities reaching up to half of the channel flow velocity (Huang et al., 2022; Lee, 2010; Verney et al., 2006; Wood et al., 1998).

Apart from affecting tidal propagation in the subtidal (permanently submerged) channel, currents over intertidal areas can directly influence the mass and momentum balance in both the channel and intertidal areas, thereby significantly affecting estuarine tidal asymmetry (Hunt et al., 2015), volume/sediment transport pathways (Kim & Cho, 2017; Luo et al., 2013), morphology (Deloffre et al., 2005), and ecology (Gordon, 1994). The lateral shear of tidal currents in the channel and intertidal zones can also enhance the differential advection of salinity and cross-shore baroclinic pressure gradients, promoting the baroclinic lateral circulation and material transport (Hendrickx & Pearson, 2024; Lerczak & Geyer, 2004). Nevertheless, due to the technical challenge and high cost of monitoring currents across vast intertidal areas, the strength of currents over intertidal areas and their impact on estuarine tidal dynamics, particularly under various estuarine and forcing conditions, remains poorly understood. This significantly restricts our ability to assess and mitigate both current and future estuarine risks arising from natural and anthropogenic changes.

This paper is Part II of a two-part theoretical study on the impact of intertidal areas on tidal propagation in tidally dominated estuaries. In Part I of this study, we developed an analytical model that dynamically resolves the coupled tidal water motions in the channel and intertidal regions for idealized tidally dominated estuaries. Unlike previous idealized, cross-sectionally averaged analytical models (e.g., Friedrichs & Madsen, 1992; Jay, 1991) that consider only the effect of intertidal areas on water storage (IWS), the model presented in Part I accounts for effects of both IWS and nonzero longitudinal currents over intertidal areas (ILC). The theoretical formulation derived in Part I demonstrates that intertidal areas affect estuarine tidal propagation by modulating the complex tidal wavenumber k through both the ratio of intertidal width to channel width (r_B) and the ratio of intertidal water flux to channel water flux (r_F), which represent the IWS and ILC effects, respectively.

This study, hereafter referred to as Part II, applies the analytical model developed in Part I to systematically investigate the strength of currents over intertidal areas and their impact on tidal propagation in idealized, tidally dominated estuaries (e.g., macro-tidal or meso-tidal during spring tides). Part II is structured as follows: Section 2 describes the research methodology; Section 3 presents the results of currents over intertidal areas and their effects on tidal propagation in the idealized Ribble estuary, along with their sensitivity to changes in estuary characteristics (e.g., length, width, depth, convergence, friction) and forcing conditions (sea-level rise, tidal forcing amplitude); Section 4 discusses the linkage between the effects of intertidal areas and the complex wavenumber and highlights the implications and limitations of our results compared to those in literature and in real estuaries; conclusions are drawn in Section 5.

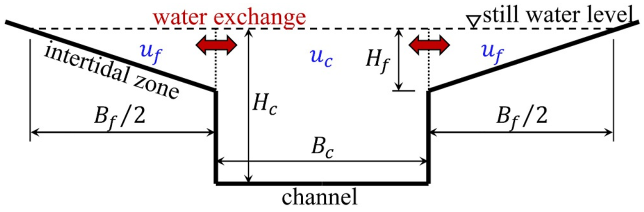

Figure 1. Diagram of an idealized estuary cross-section with a flat-bed channel and symmetric triangular intertidal areas on both sides. The channel width and depth are denoted by B_c and H_c. The parameter B_f is the width of intertidal areas at the undisturbed water level (dashed lines), and H_f is the water depth at the interface between the channel and intertidal areas (dotted lines). The variables u_c and u_f represent the along-estuary tidal velocity averaged over the channel and intertidal areas. This figure is adapted from this figure in Part I.

2. Methodology

2.1. Model Description

In our model developed in Part I, the tidal water motions in the channel and over intertidal areas are separately described by two systems of one-dimensional linearized shallow water equations averaged over the corresponding cross-section. By considering a tidally dominated condition, the effects of river discharge, nonlinear advection, horizontal mixing, and density gradients are negligible for the leading-order or principal tidal motions. Besides, the tidal amplitude at the seaward boundary, assumed to be an order of magnitude smaller than the channel depth, is also less than the water depth at the interface between the channel and intertidal areas, avoiding complete drying of intertidal areas during a tidal cycle.

For the channel area, the leading-order shallow water equations read

$$\frac{\partial}{\partial x}(u_{c_0}B_cH_c) + B_c\frac{\partial \eta_{c_0}}{\partial t} + 2F_{n_0} = 0, \tag{1a}$$

$$\frac{\partial u_{c_0}}{\partial t} = -g\frac{\partial \eta_{c_0}}{\partial x} - \frac{s_c}{H_c}u_{c_0}. \tag{1b}$$

The subscript c represents variables for the channel, whereas the subscript c_0 denotes the leading-order water motion variables in the channel. Here, x is the longitudinal coordinate, t is time, g is the acceleration of gravity, H_c is the channel water depth, B_c is the channel width, s_c is the linearized bottom friction coefficients in the channel, and u_{c_0} and η_{c_0} are the along-estuary tidal velocity and water level averaged over the channel area at the leading order. The term F_{n_0} is the lateral water exchange between the channel and intertidal areas.

For the intertidal area, the leading-order shallow water equations read

$$\frac{\partial}{\partial x}\left(u_{f_0}B_f\frac{H_f}{4}\right) + \frac{B_f}{2}\frac{\partial \eta_{f_0}}{\partial t} - F_{n_0} = 0, \tag{2a}$$

$$\frac{\partial u_{f_0}}{\partial t} = -g\frac{\partial \eta_{f_0}}{\partial x} - \frac{2s_f}{H_f}u_{f_0}. \tag{2b}$$

The subscript f represents variables for the intertidal area, and the subscript f_0 denotes the leading-order water motion variables in the intertidal area. Here, H_f is the water depth at the interface between the channel and intertidal zones, B_f is the width of intertidal areas at the undisturbed water level (see Figure 1), s_f is the linearized bottom friction coefficients in the intertidal zone, and u_{f_0} and η_{f_0} are the along-estuary leading-order tidal velocity and water level averaged over the intertidal area.

At the leading order, a periodic tidal forcing and a reflective landward boundary are imposed at the estuary mouth and head, respectively:

$$\eta_{c_0} = \eta_{f_0} = a_m\cos(\sigma t), \qquad \text{at } x = 0, \tag{3a}$$

$$u_{c_0}B_cH_c + u_{f_0}B_f\frac{H_f}{2} = 0, \qquad \text{at } x = L. \tag{3b}$$

Here, L is the estuary length, a_m is the tidal amplitude at the mouth, and σ is the tidal frequency.

Equations 1 and 2 demonstrate that the water motions in the channel and intertidal regions are dynamically coupled through the water exchange F_{n_0} (see also in Zhu et al. (2025a)). This water exchange is caused by the effects of intertidal water storage (IWS, the second term in Equation 2a) and longitudinal currents (ILC, the first term in Equation 2a) over intertidal areas. In our model, the linearized friction parameters s_c and s_f are iteratively calculated based on the prescribed drag coefficients in both regions, C_d^c and C_d^f, following the Lorentz linearization condition of the quadratic bottom stress (Hepkema et al., 2018). Large values of C_d^c and C_d^f correspond to large s_c and s_f, and strong bottom friction.

Assuming that water levels in the channel and intertidal zones are identical at the same longitudinal location (i.e., $\eta_{c_0} = \eta_{f_0}$) and neglecting Coriolis deflection, we derived an analytical solution for the leading-order tidal constituent in idealized, tidally dominated estuaries characterized by spatially uniform channel depth, exponentially convergent width, and triangular intertidal cross-sections (e.g., see Figure 1). Details of the model development are provided in Part I, and not repeated here.

Considering idealized estuaries with a periodic tidal forcing at the mouth, a free sea surface, an impermeable bottom, and a reflective landward boundary, the analytical solution for the complex tidal amplitude, $\hat{\eta}_{c_0}$, is given by:

$$\hat{\eta}_{c_0} = a_m e^{\frac{x}{2L_e}} \frac{\cosh[ik(L-x)] + (2L_e ik)^{-1} \sinh[ik(L-x)]}{\cosh(ikL) + (2L_e ik)^{-1} \sinh(ikL)}. \tag{4}$$

Here, L_e is the estuary convergence length that measures the exponential decreasing rate of the intertidal area width and channel width. The hat ($\hat{\cdot}$) indicates the complex amplitude of physical variables with its magnitude and argument equal to the amplitude and phase of tidal components (detailed in Part I). The parameter $k = k_r + ik_i$ is the complex tidal wavenumber, where its real part ($k_r > 0$) is the conventional tidal wavenumber, and its imaginary part ($k_i \leq 0$) is the damping modulus of the incident and reflected waves (Talke & Jay, 2020).

Since u_{f_0} is determined by η_{f_0} (see Equation 2), contributions of the IWS and ILC processes to the lateral water exchange F_{n_0} are physically linked. In this study, the effects of intertidal areas on tides through each process (IWS, ILC) are quantified by comparing tidal propagation using the tidal wavenumber k under three different scenarios: (a) $k = k^F$, when considering both the IWS and ILC effects, (b) $k = k^{\mathrm{IWS}}$, considering only IWS, and (c) $k = k^N$, when excluding both effects of intertidal areas:

$$k^F = \frac{2\pi}{\lambda_c}\sqrt{\frac{1+r_B}{1+r_F}\left(1 - is_c^*\right) - (\Delta_e)^2}, \tag{5a}$$

$$k^{\mathrm{IWS}} = \frac{2\pi}{\lambda_c}\sqrt{(1+r_B)\left(1 - is_c^*\right) - (\Delta_e)^2}, \tag{5b}$$

$$k^N = \frac{2\pi}{\lambda_c}\sqrt{1 - is_c^* - (\Delta_e)^2}, \tag{5c}$$

with

$$r_F = r_B \frac{H_f}{2H_c}\frac{1 - is_c^*}{1 - is_f^*}, \quad \lambda_c = \frac{2\pi}{\sigma}\sqrt{gH_c}, \quad \Delta_e = \frac{1}{2\pi}\frac{\lambda_c}{2L_e}, \quad s_c^* = \frac{s_c}{\sigma H_c}, \quad s_f^* = \frac{2s_f}{\sigma H_f}. \tag{6}$$

Here, r_B is the ratio of the intertidal area width to the channel area width, and r_F is the ratio of the complex amplitude of the longitudinal water flux integrated over the intertidal area to that integrated over the channel. The parameter λ_c represents the frictionless tidal wavelength in straight channels without any intertidal areas, Δ_e is the dimensionless convergence parameter. The parameters s_c^* and s_f^* are dimensionless linear bottom friction coefficients in the channel and intertidal areas, respectively.

2.2. Measure of the Effects of Intertidal Areas

Following Part I, the amplification factor (A_*) at the estuary head is defined by,

$$A_* = \frac{\hat{\eta}_{c_0}\big|_{x=L}}{a_m} = e^{\frac{L}{2L_e}} \frac{1}{\cosh(ikL) + (2L_e ik)^{-1}\sinh(ikL)}. \tag{7}$$

The magnitude and argument of A_* represent the amplitude ratio and the phase difference between the tidal oscillation at the head and that at the mouth, respectively. As the denominator in Equation 7 approaches zero, A_* approaches infinity, indicating the occurrence of tidal wave resonance, where the tidal amplitude significantly amplifies along the estuary.

To quantify the effects of intertidal areas on the tidal amplitude and phase within the channel, we introduce

$$\Delta A = a_m\left(\left|A_*^F\right| - \left|A_*^N\right|\right), \quad \text{and} \quad \Delta\varphi_\eta = -\arg\left(A_*^F\right) + \arg\left(A_*^N\right). \tag{8}$$

Here, A_*^F and A_*^N are the values of A_* in idealized estuaries with intertidal areas ($k = k^F$, considering both IWS and ILC effects) and those without effects of intertidal areas ($k = k^N$), respectively. For $\Delta A > 0$, intertidal areas result in an increased tidal amplitude (i.e., amplification), and vice versa. For $\Delta\varphi_\eta > 0$, intertidal areas result in delayed tidal propagation, and vice versa.

By comparing ΔA and $\Delta\varphi_\eta$ with those only considering the IWS effect (i.e., $r_F = 0$), we can also quantify the ILC effect on the tidal wave propagation with:

$$\Delta A^{\mathrm{ILC}} = a_m\left(\left|A_*^F\right| - \left|A_*^{\mathrm{IWS}}\right|\right), \quad \text{and} \ \Delta\varphi_\eta^{\mathrm{ILC}} = -\arg\left(A_*^F\right) + \arg\left(A_*^{\mathrm{IWS}}\right). \tag{9}$$

Here, A_*^{IWS} represents the value of A_* for $k = k^{\mathrm{IWS}}$. Positive values of ΔA^{ILC} and $\Delta\varphi_\eta^{\mathrm{ILC}}$ indicate amplified and delayed tides due to the ILC effect, and vice versa.

To measure the relative strength of the intertidal flow velocity, we calculated the ratio of the complex amplitudes of the intertidal flow velocity to that of the channel flow velocity (see detailed derivations in Text S1 in Supporting Information S1):

$$\frac{\hat{u}_{f_0}}{\hat{u}_{c_0}} = \frac{1 - is_c^*}{1 - is_f^*}, \tag{10}$$

with

$$U_r = \left|\frac{\hat{u}_{f_0}}{\hat{u}_{c_0}}\right| = \frac{\left|\hat{u}_{f_0}\right|}{\left|\hat{u}_{c_0}\right|}, \quad \text{and} \ \ \Delta\varphi_U = -\arg\left(\frac{\hat{u}_{f_0}}{\hat{u}_{c_0}}\right) = -\arg\left(\hat{u}_{f_0}\right) + \arg\left(\hat{u}_{c_0}\right). \tag{11}$$

Here, U_r is the absolute amplitude ratio between the intertidal and channel flow velocity, and $\Delta\varphi_U$ is their phase difference. As shown by Equation 10, in exponentially convergent estuaries with longitudinally uniform bathymetry (H_c, H_f) and bottom friction (s_c^*, s_f^*), the relative strength of the cross-sectionally averaged flow velocity in the intertidal area compared to that in the main channel remains constant throughout the estuary.

Based on the analytical solution of tidal waves (Equation 4), we can also calculate the ratio of the complex amplitudes of the lateral water exchange induced by the ILC ($\hat{F}_{n_0}^{\mathrm{ILC}}$) and IWS ($\hat{F}_{n_0}^{\mathrm{IWS}}$) effect (detailed in Text S1 in Supporting Information S1):

$$\frac{\hat{F}_{n_0}^{\mathrm{ILC}}}{\hat{F}_{n_0}^{\mathrm{IWS}}} = -\frac{1 + r_B}{r_B}\frac{r_F}{1 + r_F}. \tag{12}$$

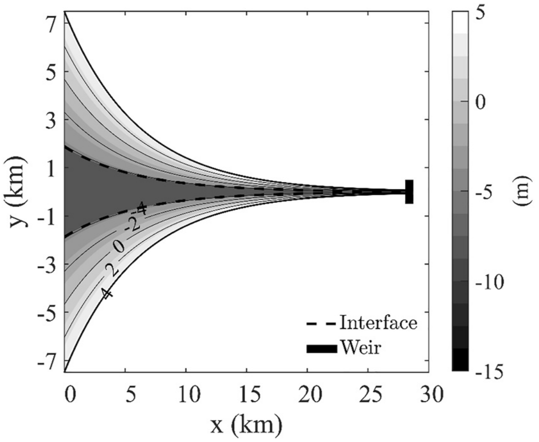

Figure 2. Geometry and bathymetry of the idealized Ribble estuary. A tidal weir is located at the estuary head. The dashed lines depict the interface between the channel and intertidal areas, where the depth H_f is defined.

Equation 12 shows that the water exchange ratio is determined by r_B and r_F, which also remains constant along the idealized estuaries considered here. The relative importance of the ILC effect on the lateral water exchange, compared to the IWS effect, is measured by

$$F_r = \left|\frac{\hat{F}_{n_0}^{\mathrm{ILC}}}{\hat{F}_{n_0}^{\mathrm{IWS}}}\right| = \frac{\left|\hat{F}_{n_0}^{\mathrm{ILC}}\right|}{\left|\hat{F}_{n_0}^{\mathrm{IWS}}\right|}, \quad \text{and} \quad \Delta\varphi_F = -\arg\left(\frac{\hat{F}_{n_0}^{\mathrm{ILC}}}{\hat{F}_{n_0}^{\mathrm{IWS}}}\right) = -\arg\left(\hat{F}_{n_0}^{\mathrm{ILC}}\right) + \arg\left(\hat{F}_{n_0}^{\mathrm{IWS}}\right). \tag{13}$$

Here, F_r represents the absolute amplitude ratio between the ILC and IWS contributions to the water exchange, and $\Delta\varphi_F$ means their phase difference. Even though U_r, F_r, $\Delta\varphi_F$, $\Delta\varphi_U$ are constant along the estuary, they can vary significantly with estuary length and other parameters that determine the complex tidal wavenumber (see Equation 5a and Section 3.2). If the channel and intertidal regions are frictionless ($s_c^* = s_f^* = 0$) or strongly frictional ($s_c^* \gg 1$; $s_f^* \gg 1$), the flux ratio r_F approaches a real number,

$$r_F = \begin{cases} r_B \dfrac{H_f}{2H_c}, & \text{for } s_c^* = s_f^* = 0 \\[2ex] r_B \dfrac{H_f}{2H_c} \dfrac{s_c^*}{s_f^*}, & \text{for } s_c^* \gg 1 \text{ and } s_f^* \gg 1 \end{cases}. \tag{14}$$

Under such conditions, the ILC-induced water exchange is precisely out of phase with the IWS-induced exchange. The non-zero longitudinal currents over intertidal areas will be referred to as intertidal currents for simplicity hereafter.

2.3. Scenario Setting

2.3.1. Default Experiment

Our default experiment considers parameters representative of the idealized Ribble estuary (UK), which is a macro-tidal estuary with a semi-diurnal (i.e., $\sigma \sim 1.4 \times 10^{-4}$ s^{-1}) tidal range of up to 8 m at the mouth and less than 4 m at the head (Admiralty, 2001; van der Wal et al., 2002). The river discharge into the Ribble estuary is below 50 m^3/s, much smaller than the tidal inflow (~12,000 m^3/s, see Burton et al. (1995)), making it a tidally dominated system (X. Li et al., 2018; Moore et al., 2009). The Ribble estuary (see Figure 2) is a short, shallow system, with a length of 28.4 km and a mean channel depth of 8 m (Luo et al., 2013). The estuary is strongly funnel-shaped, with a convergence length L_e of ~6 km. The total width significantly decreases from ~15 km at the mouth to ~100 m at the head (Dronkers, 2016). The Ribble estuary has an extensive intertidal zone with a ratio of intertidal width to channel width (r_B) of ~1.5 (van der Wal et al., 2002). Strong intertidal currents of up to ~0.4 m/s were observed near the estuary entrance (Huang et al., 2022).

In the default experiment, the water depth (H_f) at the interface between the channel and intertidal zones is set to be 0.1 m larger than the tidal amplitude at the mouth ($a_m = 4$ m), that is, $H_f = 4.1$ m (van der Wal et al., 2002), see Table 1. The bottom drag coefficients in the channel and intertidal areas are respectively set to be 0.08 and 0.10, following a large Manning's roughness coefficient (~0.2) utilized in a two-dimensional numerical model of the Ribble estuary (Boye et al., 2015; Kashefipour et al., 2002). The parameter settings for the default experiment are summarized in Table 1.

To demonstrate the performance of the analytical model developed here, we compared the tidal level and flow velocity in the idealized Ribble estuary calculated from the analytical model with those obtained from the idealized, three-dimensional (3D), semi-analytical model developed by Zhu et al. (2025a). The 3D semi-analytical model has been validated against the numerical model Delft3D, which resolves nonlinear processes

Table 1
Parameters for the Idealized Ribble Estuary

Parameter	Description	Value	Unit	Data source
L	Estuary length	28.4	km	Luo et al. (2013)
L_e	Estuary convergence length	6	km	Dronkers (2016)
H_c	Depth in the channel	8	m	Dronkers (2016)
H_f	Depth at the channel-intertidal interface	4.1	m	van der Wal et al. (2002)
r_B	Ratio of intertidal width to channel width	1.5		van der Wal et al. (2002)
a_m	Tidal amplitude at the mouth	4	m	Admiralty (2001)
σ	Tidal frequency	1.4	10^{-4} s^{-1}	van der Wal et al. (2002)
C_d^c	Channel bottom drag coefficient	0.08		Boye et al. (2015) and Kashefipour et al. (2002)
C_d^f	Intertidal bottom drag coefficient	0.10		Boye et al. (2015) and Kashefipour et al. (2002)
s_c	Linearized channel friction coefficient	0.04	m/s	Lorentz linearization
s_f	Linearized intertidal friction coefficient	0.02	m/s	Lorentz linearization

and quadratic bed friction, effects that are not considered in the semi-analytical model. The estuary parameters in the 3D semi-analytical model are identical to the default settings utilized in the cross-sectionally averaged analytical model (Table 1). In the 3D semi-analytical model, the lateral variability of the channel flow is minor due to the geometry considered in this study (a flat-bed channel), and for fair comparison with our one-dimensional analytical model, an infinitely large vertical eddy viscosity is applied in the 3D model to obtain vertically homogeneous currents.

2.3.2. Sensitivity Experiments

To systematically investigate the response of intertidal currents and their effects on the tide propagation in the channel to changes in estuary characteristics and forcing conditions, we design four groups of sensitivity experiments (I-IV), where parameters (I) L & H_c, (II) L_e & C_d^c, (III) r_B & C_d^f, and (IV) a_m & sea-level rise (denoted by η_{SLR}) are changed respectively. Since the tidal wavenumber k is a function of many of these parameters (Equation 5), the sensitivity experiments designed here cannot easily be conducted using nondimensional parameters such as Δ_e and L/λ_c. For instance, when varying the dimensionless convergence parameter Δ_e (by changing L_e and λ_c), all other terms in k are also altered due to their dependence on the channel water depth and tidal frequency. Hence, the sensitivity of effects of intertidal areas to these parameters is explored by altering one of these dimensional parameters in each experiment while keeping the other parameters at their default values as listed in Table 1.

The variation ranges of these parameters are determined by their typical values in real estuaries extracted from prior studies. In experiment group I, the ranges of the estuary length L and channel depth H_c are determined by the ratio of estuary length to the frictionless tidal wavelength: L/λ_c, which lies between 0 and 0.5 (Talke & Jay, 2020). Experiment group II explores a wide range of conditions with different relative importance of estuary convergence versus channel friction, where L_e varies between 5 and 50 km (Dronkers, 2016) and C_d^c between 0.001 and 0.1 (Austin et al., 2011; Bricker et al., 2005; Ludwick, 1975; van Prooijen & Wang, 2013). In group III, the responses of effects of intertidal areas to changes in intertidal characteristics are studied, with r_B ranging from 0 to 3 (Dronkers, 2016; Friedrichs & Aubrey, 1994) and C_d^f from 0.05 to 5 (Ashall et al., 2016; Stark et al., 2017; L. Li et al., 2012). This range of C_d^f represents strong variability of bed friction over natural intertidal areas, for example, weak friction over bare mudflats, strong friction over areas with saltmarshes and mangroves. Experiment group IV investigates the response of the effects of intertidal areas to sea-level rise (η_{SLR}) and changes in tidal forcing (a_m) due to natural or anthropogenic factors (Talke & Jay, 2020). Here, changes in sea-level rise are considered by increasing the undisturbed water level (from 0 to η_{SLR}) by up to 2 m with the bed level unchanged, and a_m changes from 2 to 4 m to cover the macro-tidal conditions. Since a_m and η_{SLR} also affect the total estuary width and depth, parameters r_B, H_c, and H_f are effectively changed in these experiments (see Text S2 and Figure

Table 2
Parameter Changes in Sensitivity Experiments

Experiment group	Sensitivity parameter	Parameter description	Value range	Unit
I	L	Estuary length	20–150	km
	H_c	Channel water depth	5–50	m
II	L_e	Estuary convergence length	5–50	km
	C_d^c	Channel bottom drag coefficient	0.001–0.1	
III	r_B	Ratio of intertidal width to channel width	0–3	
	C_d^f	Intertidal bottom drag coefficient	0.05–5	
IV	a_m	Tidal amplitude at the mouth	2–4	m
	η_{SLR}	Sea-level rise	0–2	m

S1 in Supporting Information S1). The changed parameters and their range of variations in these experiments are summarized in Table 2.

3. Results

3.1. Idealized Ribble Estuary

In the idealized Ribble estuary, the tidal water level amplitude considerably decreases landward, possibly due to strong bottom friction or shallow water depth (Figure 3a). The tidal surface phase monotonically increases along

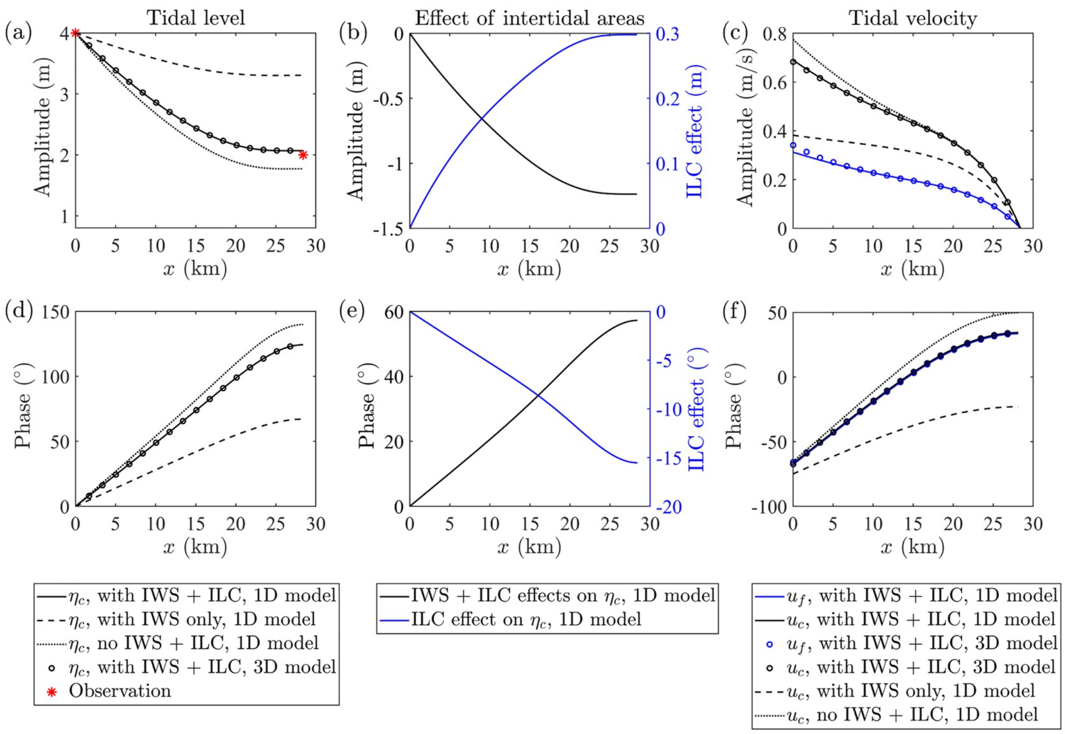

Figure 3. (a) Amplitude of the tidal surface elevation in the default experiment (Table 1) with intertidal zones (solid line), only considering the IWS effect (dotted line), and without intertidal zones (dashed line). (b) Changes in the tidal water level amplitude in the channel due to the total effect of intertidal areas (black line) and the effect of intertidal areas due to the ILC contribution only (blue line). (c) Amplitude of the channel (black line) and intertidal (blue line) flow velocity. (d–f) Same as (a–c) but for the phase. The lines represent the tidal level and flow in the idealized Ribble estuary calculated by our one-dimensional (1D) analytical model, and the circles represent the results obtained from the three-dimensional (3D), semi-analytical model of Zhu et al. (2025a). The asterisks represent the observed tidal water level amplitude at the estuary mouth and head.

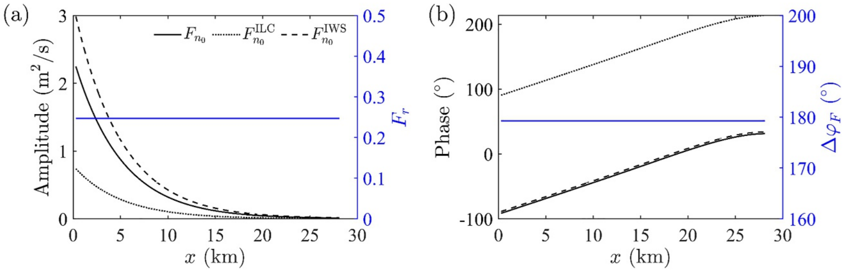

Figure 4. (a) Amplitude and (b) phase of the total water exchange between the channel and intertidal zones in the default estuary (F_{n_0}, black solid lines) and the water exchange contributions induced by the ILC ($F_{n_0}^{\mathrm{ILC}}$, black dotted lines) and IWS ($F_{n_0}^{\mathrm{IWS}}$, black dashed lines) effects [obtained from Equations S3 and S4 in Text S1 in Supporting Information S1. The blue line indicates the (a) amplitude ratio and (b) phase difference between both contributions (calculated from Equation 13).

the estuary (Figure 3d). These spatial patterns are consistent with observed tidal features along the Ribble estuary (see red asterisks in Figure 3a), where the tidal range decreases from ∼8 m at the mouth to 4 m at the head (Admiralty, 2001; van der Wal et al., 2002). The amplitude of tidal velocities in the channel and over the intertidal areas decreases landward from ∼0.7 m/s and ∼0.3 m/s at the mouth to zero at the head, respectively (Figure 3c). Phases of the tidal velocities over the channel and the intertidal area are close to each other, both of which increase monotonically toward the head (Figure 3f). The modeled peak tidal current velocities within the channel and intertidal areas also align with their typical magnitudes observed in the Ribble estuary, which are ∼0.7–1.5 m/s in the deep channel and ∼0.1–0.4 m/s over intertidal zones (Burton et al., 1995; Huang et al., 2022; Kashefipour et al., 2002; Namin et al., 2004; van der Wal et al., 2002). The along-estuary distributions of the amplitude and phase of the tidal level and flow in the channel and intertidal areas simulated using the cross-sectionally averaged analytical model also align well with results obtained from the three-dimensional, semi-analytical model of Zhu et al. (2025a) (see circles in Figures 3a, 3c, 3d, and 3f).

Tidal propagation in this estuary is significantly affected by its extensive intertidal area. The presence of intertidal zones leads to tidal damping of up to 1.2 m in the estuary (Figure 3b, black line) and a phase delay of up to 60° (Figure 3e, black line). The ILC effect, however, results in an increase in tidal water level amplitude of up to 0.3 m (Figure 3b, blue line) and a decrease in the tidal surface phase of up to 15° (Figure 3e, blue line). This means that, in the idealized Ribble estuary, the ILC effect is responsible for nearly a fourth of the total effects of intertidal areas on the tidal water level amplitude and phase. Due to the prescribed tidal forcing at the mouth, which is identical in experiments with and without intertidal areas for fair comparison, the effects of intertidal areas on the tide propagation are more pronounced in the upper reach and vanish toward the seaward boundary (Figures 3b and 3e).

Tidal currents in the channel are considerably modulated by the intertidal areas. The presence of intertidal areas tends to enhance the current velocity in the channel by up to 0.4 m/s near the mouth (compare black solid and dashed lines in Figure 3c), as also found by Zhu et al. (2025a). The ILC effect, however, leads to a decrease of up to 0.1 m/s near the mouth in tidal velocity amplitude (compare black and dotted lines in Figure 3c). The total effect of intertidal areas on the tidal velocity phase and its ILC contribution are similar to that on the phase of tidal surface elevation, causing a phase delay of up to 60° and a phase decrease of up to 15° near the estuary head (Figure 3f), respectively.

The effects of intertidal areas on the tide propagation in the channel are directly controlled by the water exchange between the channel and intertidal zones. In the idealized Ribble estuary, this water exchange decreases significantly landward (Figure 4a, black solid line). The ILC-induced exchange accounts for a fourth of the IWS-induced exchange (Figure 4a, blue line). The phase difference between water exchange contributions of IWS and ILC is ∼180° (Figure 4b, blue line), indicating that they are almost out of phase. This means that the ILC-induced water exchange compensates for ∼25% of the IWS-induced exchange along the estuary, effectively reducing the total water exchange (as seen by comparing black solid and dashed lines in Figure 4a). This explains why the IWS and ILC effects of intertidal areas on the tidal water level amplitude and phase partially counteract each other (Figure 3), confirming a significant impact of strong intertidal currents on the tide propagation in the channel.

3.2. Sensitivity Studies

To understand the significance of intertidal currents and their effects on tidal propagation under various estuarine conditions, we conducted four groups of experiments to explore their sensitivity to L, H_c, L_e, C_d^c, r_B, C_d^f, a_m, and η_{SLR} (see Section 2.3.2 and Table 2), with the other parameters kept at their default values (Table 1). For each group of experiments, the responses of the ratio between intertidal and channel flow velocities, the ratio between the ILC- and IWS-induced lateral water exchange, and the effects of intertidal areas on the tidal amplification or damping to changes in each of these parameters are presented below. The along-estuary distributions of the effects of intertidal areas and the tidal changes in the middle estuary (see Text S3 and Figures S2–S6 in Supporting Information S1) demonstrate that the roles of intertidal areas in modulating tides are most pronounced near the head of the convergent estuaries considered in this study, as also found by Talke and Jay (2020). Also, these effects of intertidal areas can vary significantly between tidal amplification and damping across estuaries with different parameters. For simplicity, the sensitivity analysis below focuses mainly on the tidal change at the estuary head induced by intertidal areas.

3.2.1. Estuary Length and Channel Depth

Both estuary length (L) and channel depth (H_c) affect tide propagation through modulating the nondimensional tidal wavenumber kL, as shown by Equation 4 and Friedrichs and Madsen (1992). The channel depth H_c influences the complex tidal wavenumber (k) in multiple ways. As shown in Equations 5 and 6, changes in H_c affect k by modulating the frictionless tidal wavelength (λ_c), the ratio of the intertidal cross-sectional flux to the channel cross-sectional flux (r_F), and the dimensionless linearized bottom friction coefficient in the channel (s_c^*).

Our sensitivity results from experiment group I confirm that the intertidal currents and their effect on tide propagation are strongly dependent on L and H_c (Figure 5). The relative strength of the intertidal current velocity with respect to channel flow velocity (U_r) significantly increases from ~0.2 to 0.5 as H_c decreases from 50 to 5 m (Figure 5a). The amplitude of intertidal current velocity is around 0.1–0.4 m/s at the estuary mouth, which mainly increases as H_c decreases (not shown). The relative strength of intertidal currents is less sensitive to the estuary length compared to the channel depth. The ratio between the ILC- and IWS-induced water exchange (F_r) only slightly changes with L, but it considerably increases from ~0.1 to 0.4 as H_c decreases (Figure 5b). Decreases in H_c also cause the phase difference ($\Delta\varphi_F$) to increase from ~160° to 180° (not shown here), which means the ILC- and IWS-induced water exchanges are almost out of phase.

The effects of intertidal areas on tidal amplification/damping are also strongly modulated by L and H_c. For $H_c <$ ~20m, the inclusion of intertidal areas leads to a decrease in the tidal amplitude at the head of up to 2 m. For larger H_c, however, it leads to an increase in tidal amplitude of up to 0.3 m (Figure 5c). Regardless of the values of L and H_c, the tide propagation is always delayed (by more than 100°) by intertidal areas (Figure 5d), as found by Jay (1991). The phase delay caused by the effects of intertidal areas increases as H_c decreases. The above-mentioned effects of intertidal areas become even more pronounced when considering a larger L.

In contrast to the total effects of intertidal areas (and the IWS effect), the ILC effect tends to increase the tidal amplitude (by up to 0.45 m) for $H_c <$ ~20 m and reduce it (by less than 0.05 m) for larger H_c (Figure 5e). The ILC effect also leads to a decrease in the tidal phase of more than 50° (Figure 5f), meaning that the delaying effect of intertidal areas on the tidal propagation is reduced when taking into account longitudinal currents over intertidal areas. This ILC effect counteracts up to 40% of the total effect of intertidal areas, and is more significant when considering a smaller H_c.

3.2.2. Convergence Length and Channel Bottom Friction

The complex tidal wavenumber (k) is also strongly affected by estuary convergence (L_e) and channel bottom friction (C_d^c). As Equation 5 shows, L_e influences the convergence term L_e/λ_c, while C_d^c affects both the ratio of intertidal water flux to that in the channel (r_F) and the dimensionless linearized bottom friction coefficient in the channel (s_c^*).

Our results from experiment group II show that the intertidal currents and their effect on tides are sensitive to both L_e and C_d^c (Figure 6). The ratio of intertidal flow velocity to the channel flow velocity (U_r) shows very weak sensitivity to L_e, but it significantly increases from ~0.1 to 0.5 as C_d^c increases from 0.001 to 0.1 (Figure 6a). The

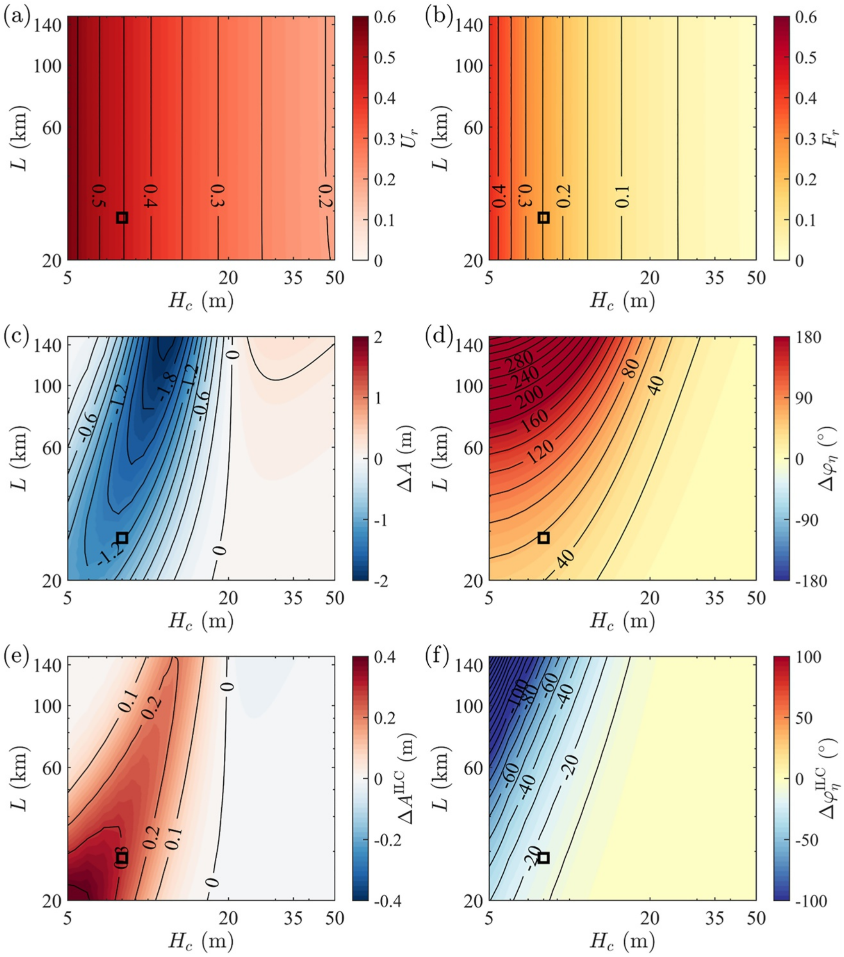

Figure 5. Sensitivity of (a) the ratio between the intertidal and channel flow velocities U_r, (b) the ratio between the ILC- and IWS-induced water exchange F_r, (c) effects of intertidal areas on the tidal amplitude ΔA, (d) effects of intertidal areas on the tidal phase $\Delta\varphi_\eta$, (e) ILC effects on the tidal amplitude ΔA^{ILC}, and (f) ILC effects on the tidal phase $\Delta\varphi_\eta^{\mathrm{ILC}}$ to the estuary length L and channel depth H_c. The black squares depict the default values as given in Table 1. The x and y axes are logarithmic for readability.

peak intertidal current speed is around 0.1–0.45 m/s near the mouth, which increases as L_e and C_d^c increase (not shown). The ratio between the ILC- and IWS-induced water exchange (F_r) is almost independent of L_e, but it increases from ∼0.05 to 0.3 as C_d^c increases (Figure 6b). The increases in C_d^c result in an increase in the phase difference ($\Delta\varphi_F$) from ∼130° to 180° (not shown here).

The effects of intertidal areas on tidal amplification/damping at the estuary head are strongly modulated by both L_e and C_d^c. In estuaries with a strong width convergence and weak bottom friction in the channel (i.e., small L_e and C_d^c), intertidal areas cause tidal amplification by up to 0.3 m at the head (Figure 6c). In weakly convergent estuaries with strong bottom friction in the channel (i.e., large L_e and C_d^c), however, the intertidal zone results in tidal damping by more than 1.2 m. The tidal phase is delayed by ∼10°–60° as a result of intertidal areas (Figure 6d), which increases with increasing C_d^c and/or L_e.

Similar to experiment group I, the ILC effect makes an opposite contribution to the tidal oscillations compared to the total effects of intertidal areas. For small L_e and C_d^c, the ILC effect leads to tidal damping by less than 0.05 m; for large L_e and C_d^c, the ILC effect leads to tidal amplification by up to 0.35 m (Figure 6e). Depending on the estuary convergence and channel bottom friction, the ILC effect can reduce the tidal phase delay by up to 18° in the channel (Figure 6f). The ILC effect counterbalances up to approximately 30% of the effect of intertidal areas on tidal amplitude or phase for larger C_d^c.

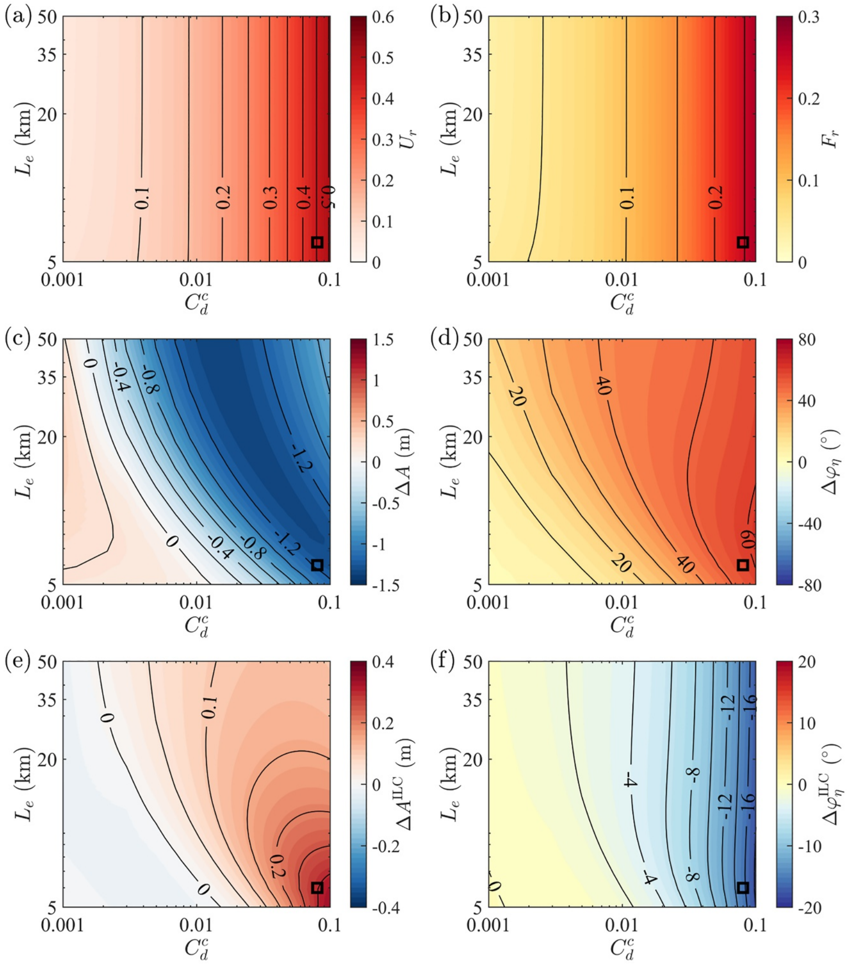

Figure 6. Sensitivity of (a) the ratio between the intertidal and channel flow velocities U_r, (b) the ratio between the ILC- and IWS-induced water exchange F_r, (c) effects of intertidal areas on the tidal amplitude ΔA, (d) effects of intertidal areas on the tidal phase $\Delta\varphi_\eta$, (e) ILC effects on the tidal amplitude $\Delta\mathrm{A}^{\mathrm{ILC}}$, and (f) ILC effects on the tidal phase $\Delta\varphi_\eta^{\mathrm{ILC}}$ to the convergence length L_e and channel drag coefficient C_d^c. The black squares depict the default values as given in Table 1. The *x* and *y* axes are logarithmic for readability.

3.2.3. Intertidal Width and Bottom Friction

Equation 5 also suggests that the changes in the width and bottom friction over the intertidal areas affect the complex tidal wavenumber (k) through modulating the ratio of intertidal width to channel width (r_B) and the ratio of intertidal water flux to that in the channel (r_F). The latter ratio is strongly affected by the intertidal bottom friction (C_d^f).

Our results from experiment group III show different sensitivities of the intertidal currents and their effects on tides to r_B and C_d^f (Figure 7). The ratio of intertidal flow velocity to channel flow velocity (U_r) remains nearly unchanged with r_B, but it increases considerably from ~0.1 to 0.6 as C_d^f decreases from 5 to 0.05 (Figure 7a). The maximum intertidal current velocity is around 0.05–0.5 m/s at the mouth, which increases as C_d^f decreases or r_B increases (not shown). The ratio between the ILC- and IWS-induced water exchange (F_r) increases from ~0.05 to 0.45 with increasing r_B and decreasing C_d^f (Figure 7b). The phase difference ($\Delta\varphi_F$), however, remains almost unchanged at around 180° (not shown here). This again confirms that the ILC-induced exchange is almost out of phase with the IWS-induced exchange.

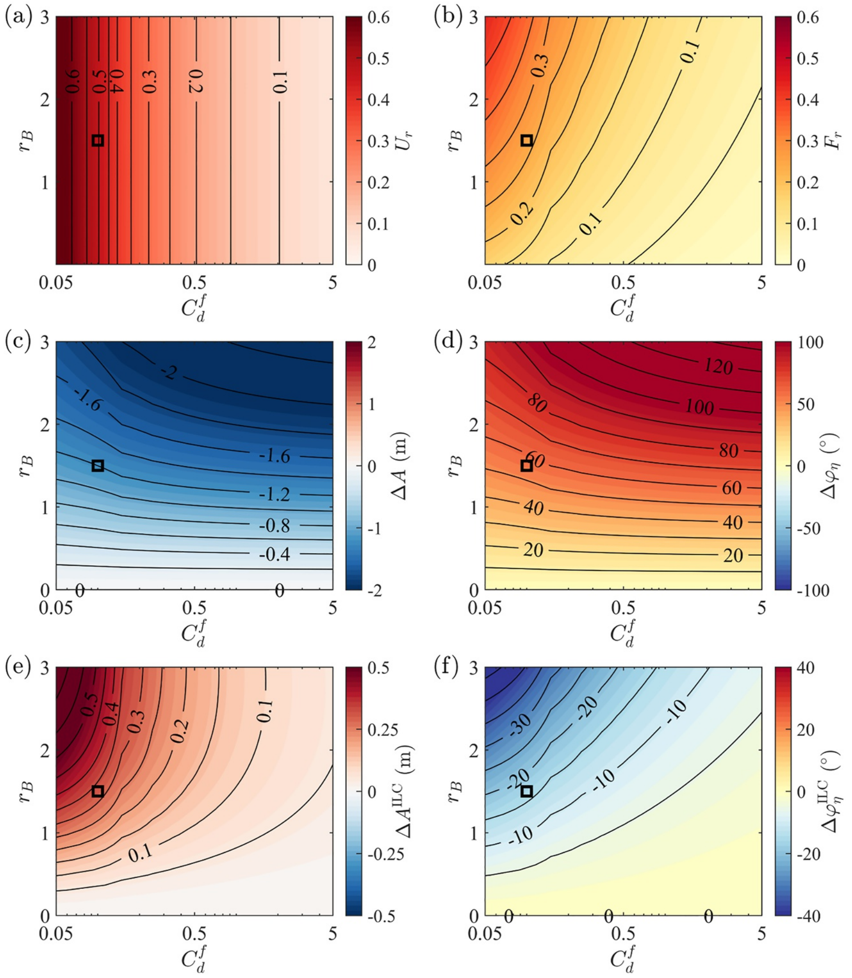

Figure 7. Sensitivity of (a) the ratio between the intertidal and channel flow velocities U_r, (b) the ratio between the ILC- and IWS-induced water exchange F_r, (c) effects of intertidal areas on the tidal amplitude ΔA, (d) effects of intertidal areas on the tidal phase $\Delta\varphi_\eta$, (e) ILC effects on the tidal amplitude $\Delta \mathrm{A}^{\mathrm{ILC}}$, and (f) ILC effects on the tidal phase $\Delta\varphi_\eta^{\mathrm{ILC}}$ to the ratio of intertidal width to channel width r_B and intertidal drag coefficient C_d^f. The black squares depict the default values as given in Table 1. The x axis is logarithmic for readability.

The effects of intertidal areas on the tide propagation are also strongly affected by r_B and C_d^f. Regardless of the values of r_B and C_d^f, the intertidal areas cause tidal damping at the head by up to 2 m (Figure 7c) and delayed tidal propagation by more than 100° (Figure 7d). These total effects of intertidal areas are more pronounced with increasing r_B and C_d^f. The ILC effect, however, induces tidal amplification by up to 0.6 m (Figure 7e) and advances tidal propagation by up to 50° (Figure 7f). The ILC effect increases as r_B increases or C_d^f decreases, counterbalancing up to 45% of the effect of intertidal areas on tidal damping and phase delay at the head.

3.2.4. Tidal Forcing and Sea-Level Rise

Changes in the tidal forcing a_m and sea-level rise η_{SLR} result in different changes in the width (B_c, B_f) and mean depth (H_c, H_f) of the channel and intertidal regions, thus modulating the width ratio r_B and water flux ratio r_F between the two regions, as well as the complex tidal wavenumber k (see Equations 5 and 6).

Our results from experiment group IV confirm strong sensitivity of the intertidal currents and their effect on tides to a_m and η_{SLR} (Figure 8). The ratio of intertidal flow velocity to channel velocity (U_r) considerably decreases from ~0.45 to 0.35 as a_m decreases from 4 to 2 m, although it only slightly decreases with increasing η_{SLR} to 2 m (Figure 8a). The peak intertidal current speed is around 0.1–0.3 m/s at the mouth, which significantly increases as

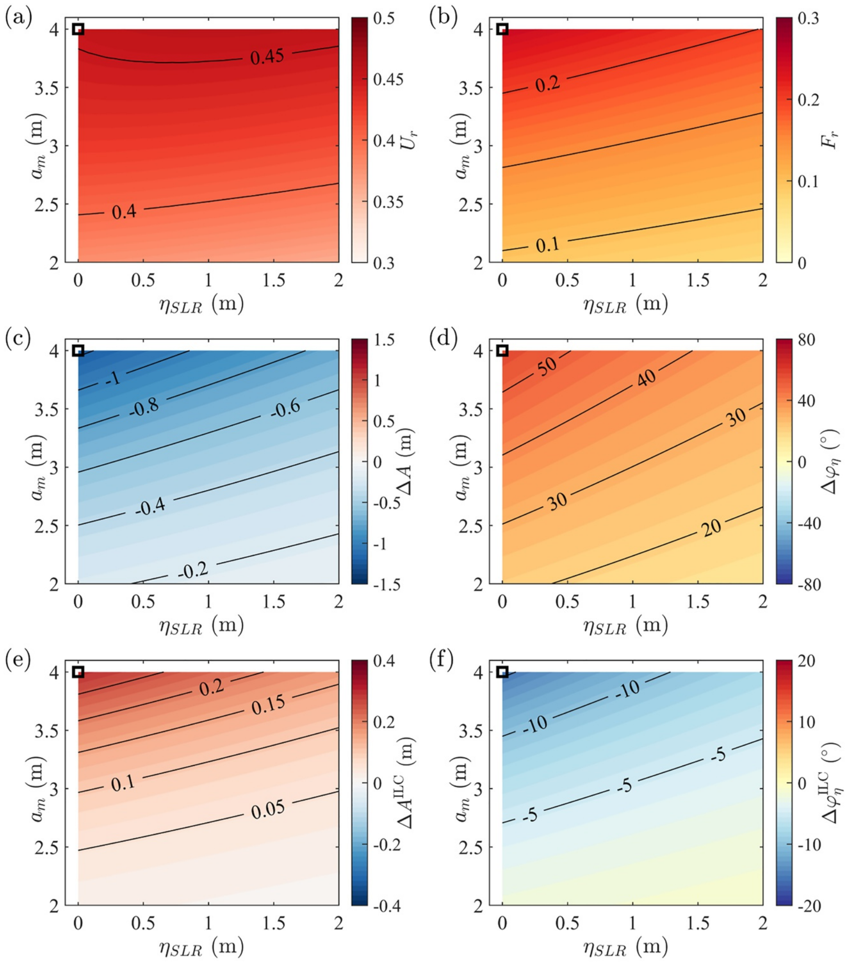

Figure 8. Sensitivity of (a) the ratio between the intertidal and channel flow velocities U_r, (b) the ratio between the ILC- and IWS-induced water exchange F_r, (c) effects of intertidal areas on the tidal amplitude ΔA, (d) effects of intertidal areas on the tidal phase $\Delta\varphi_\eta$, (e) ILC effects on the tidal amplitude ΔA^{ILC}, and (f) ILC effects on the tidal phase $\Delta\varphi_\eta^{\mathrm{ILC}}$ to the tidal amplitude at the mouth a_m and sea-level rise η_{SLR}. The black squares depict the default values as given in Table 1.

a_m increases but slightly decreases as η_{SLR} increases (not shown). This again confirms that strong intertidal currents can occur in estuaries with a large tidal range (e.g., meso-tidal estuaries during spring tides or macro-tidal estuaries). The amplitude ratio between the ILC- and IWS-induced water exchange (F_r) decreases from ~0.25 to 0.05 with increasing η_{SLR} or decreasing a_m (Figure 8b). The phase difference between the two water exchange components ($\Delta\varphi_F$) remains around 180^0 (not shown here).

The effects of intertidal areas on tidal propagation in the channel are also strongly modulated by a_m and η_{SLR}. The inclusion of intertidal areas leads to tidal damping, reducing the tidal amplitude by up to 1.2 m (Figure 8c) and increasing the tidal phase by up to 60° (Figure 8d). These total effects of intertidal areas become less pronounced with an increase in η_{SLR} or a decrease in a_m. The ILC effect, however, causes tidal amplification by up to 0.3 m (Figure 8e) and advanced tidal propagation by up to 15° (Figure 8f). The ILC effect increases as a_m increases or η_{SLR} decreases, counterbalancing up to 25% of the effect of intertidal areas on the tidal amplitude and phase at the estuary head.

The sensitivity of the total effect of intertidal areas on tidal propagation and its ILC contribution to the tidal amplitude at the mouth (a_m) and sea-level rise (η_{SLR}) can be largely explained by their dependence on the ratio of intertidal width to channel width r_B (see Figures S1b and S1c in Supporting Information S1). As increasing η_{SLR} and/or decreasing a_m tend to decrease r_B (Figure S1b in Supporting Information S1), both the total effects of intertidal areas and the ILC contribution become less pronounced as sea level rises or tidal range decreases (Figures 7c–7f and 8c–8f).

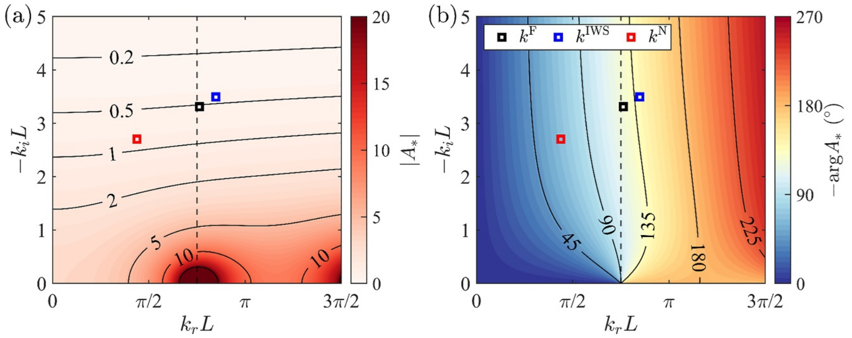

Figure 9. (a) Amplitude and (b) phase of A_* (obtained from Equation 7) as a function of k_rL and $-k_iL$ for the default value of $L_e/L = 0.2$. The black dashed line shows the value of k_rL under the resonance condition ($|A_*| \to \infty$). The squares represent the tidal wavenumber of the default idealized Ribble estuary with intertidal zones (black), considering only the IWS effect (blue), and without intertidal zones (red). This figure is adapted from Figure 3 in Part I.

4. Discussion

4.1. Tidal Wavenumber

The effects of intertidal areas on tidal propagation in the idealized Ribble estuary and the sensitivity of tidal amplification/damping to various estuary parameters can be explained by the influences of these estuary parameters on the nondimensional tidal wavenumber kL and L_e/L. Figure 9 shows that for a default estuary convergence ($L_e/L = 0.2$), resonance ($|A_*| \to \infty$) occurs at $k_rL \sim 3\pi/4$ or $2\pi > k_rL > 3\pi/2$, with $k_iL = 0$. As real estuaries are rarely influenced by the second resonance mode (Talke & Jay, 2020), the discussion hereafter focuses on the impact of the first resonance mode at $k_rL \sim 3\pi/4$.

The effects of intertidal areas on tidal motions and their sensitivity to various estuary parameters, as shown in Section 3, can be explained by the distance between the tidal wavenumber (k_rL, $-k_iL$) and its resonant value ($|A_*| \to \infty$) in each experiment. When k_rL falls below its resonant value, increasing k_rL leads to tidal amplification (i.e., increased $|A_*|$), and vice versa (Figure 9a). When k_rL exceeds its resonant value, however, increasing k_rL leads to tidal damping (i.e., decreased $|A_*|$). Since the damping modulus k_i measures the exponential decay rate of the incident and reflected waves, an increase in $-k_iL$ causes tidal damping by decreasing $|A_*|$. Besides, increasing k_rL results in delayed tidal propagation (i.e., increased $\arg A_*$), whereas increasing $-k_iL$ can cause either delayed or advanced (i.e., decreased $\arg A_*$) tidal propagation depending on k_rL (Figure 9b).

In Part I of this study, the sensitivity of the wavenumber to several nondimensional parameters (e.g., $H_f/2H_c$, L/λ_c) is investigated in seven specific systems classified by the relative dominance of local inertia, width convergence, and bottom friction. As discussed in Part I (e.g., its Figure 4), intertidal zones affect both the real (k_rL) and imaginary (k_iL) parts of the nondimensional tidal wavenumber (kL), which are sensitive to various estuarine parameters, through the width and water flux ratios between the intertidal and channel regions (r_B and r_F). Here in Part II, however, the response of the wavenumber to various dimensional parameters (e.g., L, H_c) is further examined based on the default setting of the idealized Ribble estuary, which offers a direct understanding of how the wavenumber changes with different estuary parameters. As shown in Figure 10, k_rL and $-k_iL$ increase with increasing L, C_d^c, C_d^f, r_B, or decreasing H_c, while increasing L_e results in an increase in k_rL and a decrease in $-k_iL$. The sensitivity of the wavenumber to the tidal amplitude at the mouth (a_m) and sea-level rise (η_{SLR}) can be largely explained by their influence on r_B (as also demonstrated in Section 3.2.4), not shown here.

Comparing solid lines with dashed or dotted lines in Figure 10, we found that intertidal zones increase k_rL and $-k_iL$, while the ILC effect reduces both parameters. Under conditions of small kL, where k_rL is less than its resonant value (red lines), such as with large H_c or small L, C_d^c, L_e, an increase in k_rL induced by intertidal zones leads to tidal amplification (closer to resonance and increased $|A_*|$), while the ILC effect causes tidal damping (by decreasing k_rL, Figure 10). Conversely, under conditions of large kL, where k_rL exceeds its resonant threshold, increases in both k_rL and $-k_iL$ induced by intertidal zones causes tidal damping (decreased $|A_*|$). The ILC effect, however, reduces both k_rL and $-k_iL$, causing tidal amplification.

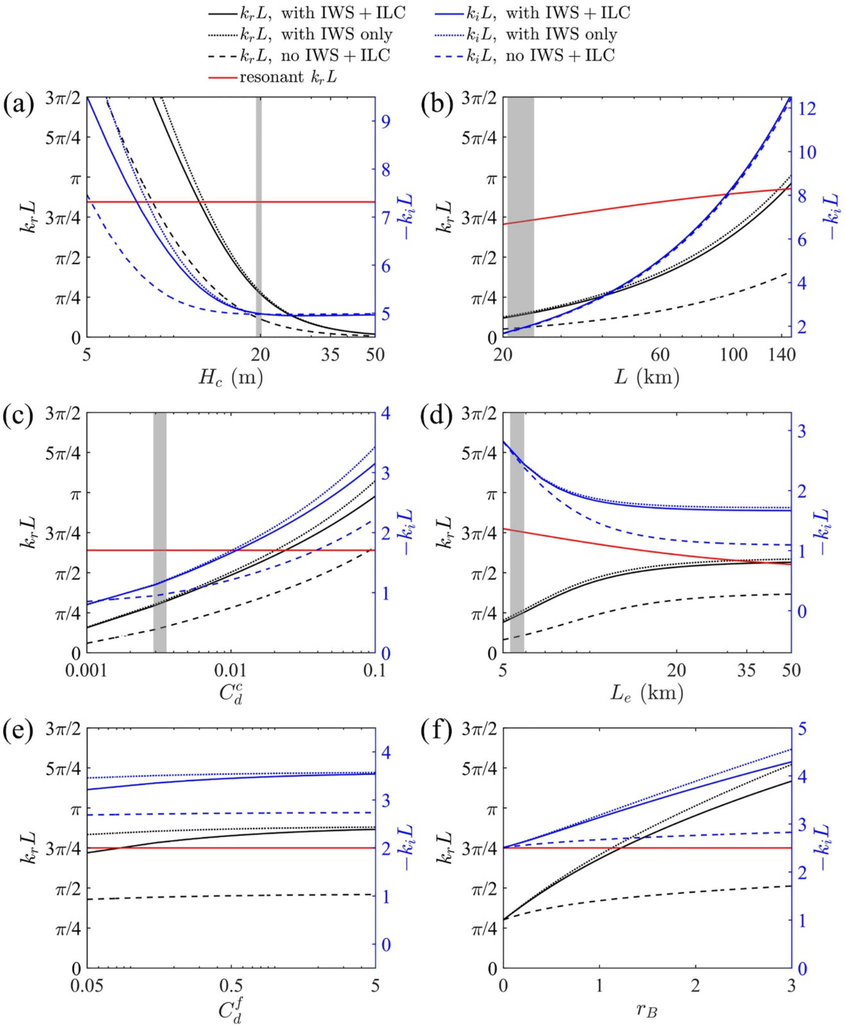

Figure 10. Changes in k_rL (black) and $-k_iL$ (blue) with (a) the channel water depth H_c with $L = 60$ km, (b) estuary length L with $H_c = 18$ m, (c) channel bottom drag coefficient C_d^c with $L_e = 15$ km, (d) estuarine convergence length L_e with $C_d^c = 0.01$, (e) intertidal bottom drag coefficient C_d^f with $r_B = 1.5$, and (f) ratio of intertidal width to channel width r_B with $C_d^f = 0.5$. Other parameters in each sensitivity scenario are the same as those in the default experiment. Red lines indicate the values of the resonant k_rL as a function of L_e/L calculated from $|A_*| \to \infty$. Gray areas represent the transition between tidal amplification (increased $|A_*|$) and damping (decreased $|A_*|$) due to the total effect of intertidal areas and/or the ILC effect extracted from the results in Section 3.2.

Figure 10 also highlights that the relative importance of the ILC effect (comparing black solid and dotted lines) to tidal propagation is more pronounced under conditions of larger kL, such as shallower water depth, longer estuary length, stronger bottom friction within the channel, weaker width convergence, or larger intertidal width, but with weaker intertidal bottom friction. These conditions correspond to a large water flux ratio between intertidal and channel regions (r_F, defined in Equation 6), where the intertidal flow velocities can reach up to 60% of the flow velocity in the channel (see Section 3.2).

Since the Ribble estuary is a strongly dissipative and strongly convergent system with a large kL (see squares in Figure 9, where $-k_iL > k_rL$ as classified in Part I) and the tide is strongly damped landward (Figure 3a), the increase in kL caused by the total effects of intertidal areas makes the system less resonant (decreased $|A_*|$). However, the decrease in kL due to the ILC contribution brings the system slightly closer to resonance (increased $|A_*|$). This explains why the semi-diurnal tide in the Ribble estuary is dampened by the intertidal zones but amplified by the ILC effect (Figure 3b). In strongly frictional estuaries such as the Ribble estuary (i.e., large C_d^c) where the incident and reflected tidal waves decay very fast along their traveling directions, the damping modulus

$-k_iL$ is large (Figure 10c) and the magnitude of the amplification factor ($|A_*|$) changes only slightly with k_rL (Figure 9a). Hence, in these estuaries, the tidal damping induced by the inclusion of intertidal areas (Figure 6c) is mostly associated with the increase in $-k_iL$, whereas the tidal amplification induced by the ILC effect (Figure 6e) is primarily linked to the decrease in $-k_iL$.

As intertidal areas always tend to increase k_rL and $-k_iL$, they lead to delayed tidal propagation in all experiments (Section 3.2). The ILC effect, however, reduces the tidal wavenumber and results in advanced tidal propagation (see Figures 9b and 10).

4.2. Implications and Limitations

The physical mechanisms revealed in Section 4.1 are useful to understand the contrasting effects of intertidal zones on tidal propagation in natural tidally dominated estuaries, such as those discussed in the introduction. In long, shallow semi-enclosed systems such as the Scheldt estuary (e.g., with a length of more than ∼100 km and a depth of less than ∼10 m), k_rL is large and exceeds its resonant value. Hence, its intertidal zone leads to tidal damping (Stark et al., 2017). In short systems like Xiangshan Bay and Darwin Harbor (e.g., with $L < \sim 50$ km), where k_rL is smaller than its resonant threshold, the intertidal areas cause tidal amplification (L. Li et al., 2012; L. Li et al., 2018). Although the Ribble estuary is short ($L \sim 30$ km), it is frictionally dominated with a large $-k_iL$ (Figure 9). Hence, its intertidal areas cause tidal damping. The Cook Inlet is very deep with a large depth of ∼50 m and a small k_rL (below its resonance threshold). Hence, its intertidal areas lead to tidal amplification (Oey et al., 2007).

However, to allow for an analytical solution, our model is constrained by several specific assumptions, including linearized bottom friction and the neglect of advection, river discharge, and density gradients. Also, the analytical model is limited to simplified/idealized geometry and bathymetry, represented by an exponentially convergent estuary with a deep flat-bed channel and triangular intertidal areas (see Figure 1). Besides, comprehensive comparisons between our model results and field observations have not been possible due to the lack of estuary-scale measurements of flow conditions over intertidal zones in most estuaries. Nevertheless, our analytical model demonstrates good agreement with a three-dimensional, semi-analytical model, which has been validated by Zhu et al. (2025a), in reproducing tidal levels and flow velocities in the channel and intertidal areas. More importantly, our model offers an effective approach for estimating the strength of intertidal currents and their impact on tidal propagation in real estuaries, providing valuable guidance for improving future estuarine monitoring and modeling. For example, our analytical solution shows that the relative importance of longitudinal currents over intertidal areas to tidal propagation is measured by the ratio between the ILC- and IWS-induced water exchange. This ratio can be obtained by estimating values of r_B and r_F (Equation 12) using the information of the domain-averaged channel depth, intertidal water depth, width, and bottom friction parameters.

Our sensitivity results (Section 3.2) show that channel shallowing (e.g., due to sediment deposition) and/or enhanced channel bed friction can increase the impact of intertidal currents on tides, potentially triggering the shift of the ILC effects from tidal damping to amplification. Such shift can also occur with changes in estuarine geometry, such as alterations in estuary length and width induced by relocation/construction of physical barriers and estuary embankment. Moreover, changes in the characteristics of intertidal zones, such as the bedform, vegetation, bed elevation, and width (e.g., due to reclamation/restoration of intertidal areas), can also strongly affect the strength of intertidal currents. Lastly, changes in the tidal forcing at the seaward boundary and sea-level rise (e.g., due to climate change) can modify the width ratio between the channel and intertidal areas, thus modulating the intertidal currents and their impact on estuarine tide propagation.

5. Conclusions

In this work (Part II), we systematically investigated the sensitivity of the strength of longitudinal currents over intertidal areas (ILC) and their effects on tidal propagation to various estuary characteristics (length, width, depth, convergence, friction) and forcing conditions (sea-level rise, tidal forcing amplitude) in idealized, tidally dominated estuaries with simplified geometry and bathymetry. This was conducted by using a one-dimensional analytical model developed in Part I that considers both the effects of water storage over intertidal areas (IWS) and ILC, based on the default setting of the idealized Ribble estuary (UK).

By assuming exponentially convergent width with a deep flat-bed channel and triangular intertidal areas, our analytical model was first applied to the idealized Ribble estuary. The results show that intertidal zones significantly attenuate the dominant semi-diurnal tide by up to 1.2 m and cause a phase delay of up to 60° within the estuary. This suggests the potential effectiveness of intertidal habitat restoration for mitigating flood hazards in this region. The intertidal flow velocities are up to 0.3 m/s in the lower estuary. These currents offset ∼25% of the IWS-induced water exchange and counterbalance nearly a fourth of the total effect of intertidal areas on the tidal amplitude and phase, increasing the tidal amplitude by up to 0.3 m and decreasing the tidal phase by up to 15° in the upper estuary. This implies that neglecting the ILC effect can considerably underestimate the tidal amplitude and overestimate the flood mitigation potential of managed realignment for the upper estuary.

Sensitivity results show that, in the estuaries considered in this study, the effects of intertidal areas result in tidal amplification in systems with large channel water depth, short estuary length, weak channel bottom friction, and strong estuary convergence. Conversely, the intertidal area tends to dampen tides in systems with small channel water depth, long estuary length, strong channel bottom friction, and weak estuary convergence. Moreover, the existence of intertidal zones consistently results in delayed tidal wave propagation in estuaries. Our results also show significant longitudinal currents over the intertidal areas in tidally dominated estuaries, particularly under conditions of small channel water depth, strong channel bottom friction, and weak intertidal bottom friction. These currents can reach up to 60% of the flow velocity in the channel, and the ILC effect as a result of these significant currents over intertidal areas contributes up to 45% of the total effects of intertidal areas on tidal propagation. This, in turn, reduces the lateral water exchange between the channel and intertidal areas, because the exchange induced by the ILC effect is almost out of phase with that induced by the IWS effect, and tends to advance tidal wave propagation in estuaries. As a result, the ILC effect partly counterbalances the above-mentioned effects of intertidal areas on both tidal amplitude and phase.

The significance of along-estuary currents over intertidal areas to tidal propagation in tidally dominated estuaries underscores the needs for considering currents over intertidal areas in understanding and predicting estuarine circulation, material transport and morphological evolution. This is particularly crucial in meso- and macro-tidal estuaries where intertidal areas are significantly altered by climate change and human activities. The strong sensitivity of effects of intertidal areas on tides to both channel and intertidal characteristics, as demonstrated by our study, also highlights the varying role of intertidal zones in estuarine tidal propagation. These findings have important implications for assessing climate change risks in estuarine environments and formulating strategic estuary management plans.

Conflict of Interest

The authors declare no conflicts of interest relevant to this study.

Data Availability Statement

The source code for the analytical tide model and the processing code for the analytical model results used in this study are available on Zenodo (Zhu et al., 2025b).

Acknowledgments
This work was funded by the National Natural Science Foundation of China (NSFC, 42576156, U2040203), the Key Laboratory of Ministry of Education for Coastal Disaster and Protection, Hohai University (J202201), the Fundamental Research Funds for the Central Universities (B240205032), the China Scholarship Council (CSC, File 202406710099), and the UK Natural Environment Research Council (CHAMFER project, NE/W004992/1). This work was also supported by the Open Research Fund Program of State Key Laboratory of Water Disaster Prevention (2024491011).

References

Admiralty. (2001). *Admiralty tide tables: United Kingdom and Ireland (including European Channel Ports)* (Vol. 1). United Kingdom Hydrographic Office.

Ashall, L. M., Mulligan, R. P., van Proosdij, D., & Poirier, E. (2016). Application and validation of a three-dimensional hydrodynamic model of a macrotidal salt marsh. *Coastal Engineering*, *114*, 35–46. https://doi.org/10.1016/j.coastaleng.2016.04.005

Austin, M. J., Masselink, G., Russell, P. E., Turner, I. L., & Blenkinsopp, C. E. (2011). Alongshore fluid motions in the swash zone of a sandy and gravel beach. *Coastal Engineering*, *58*(8), 690–705. https://doi.org/10.1016/j.coastaleng.2011.03.004

Boye, B. A., Falconer, R. A., & Akande, K. (2015). Integrated water quality modelling: Application to the Ribble Basin, U.K. *Journal of Hydro-Environment Research*, *9*(2), 187–199. https://doi.org/10.1016/j.jher.2014.07.002

Bricker, J. D., Inagaki, S., & Monismith, S. G. (2005). Bed drag coefficient variability under wind waves in a tidal estuary. *Journal of Hydraulic Engineering*, *131*(6), 497–508. https://doi.org/10.1061/(ASCE)0733-9429(2005)131:6(497)

Burton, D. J., West, J. R., Horsington, R. W., & Randle, K. (1995). Modelling transport processes in the Ribble Estuary. *Environment International*, *21*(2), 131–141. https://doi.org/10.1016/0160-4120(95)00003-8

Cundy, A. B., Lafite, R., Taylor, J. A., Hopkinson, L., Deloffre, J., Charman, R., et al. (2007). Sediment transfer and accumulation in two contrasting salt marsh/mudflat systems: The Seine Estuary (France) and the Medway Estuary (UK). *Hydrobiologia*, *588*(1), 125–134. https://doi.org/10.1007/s10750-007-0657-y

Deloffre, J., Lafite, R., Lesueur, P., Lesourd, S., Verney, R., & Guézennec, L. (2005). Sedimentary processes on an intertidal mudflat in the upper macrotidal Seine Estuary, France. *Estuarine, Coastal and Shelf Science*, *64*(4), 710–720. https://doi.org/10.1016/j.ecss.2005.04.004

Dronkers, J. (2016). Dynamics of coastal systems. *World Scientific*.

Friedrichs, C. T., & Aubrey, D. G. (1994). Tidal propagation in strongly convergent channels. *Journal of Geophysical Research*, *99*(C2), 3321–3336. https://doi.org/10.1029/93JC03219

Friedrichs, C. T., & Madsen, O. S. (1992). Nonlinear diffusion of the tidal signal in frictionally dominated embayments. *Journal of Geophysical Research*, *97*(C4), 5637–5650. https://doi.org/10.1029/92JC00354

Giese, B. S., & Jay, D. A. (1989). Modelling tidal energetics of the Columbia River Estuary. *Estuarine, Coastal and Shelf Science*, *29*(6), 549–571. https://doi.org/10.1016/0272-7714(89)90010-3

Gordon, D. C. (1994). Intertidal ecology and potential power impacts, Bay of Fundy, Canada. *Biological Journal of the Linnean Society*, *51*(1–2), 17–23. https://doi.org/10.1111/j.1095-8312.1994.tb00940.x

Hendrickx, G. G., & Pearson, S. G. (2024). On the effects of intertidal area on estuarine salt intrusion. *Journal of Geophysical Research: Oceans*, *129*(9), e2023JC020750. https://doi.org/10.1029/2023JC020750

Hepkema, T. M., de Swart, H. E., Zagaris, A., & Duran Matute, M. (2018). Sensitivity of tidal characteristics in double inlet systems to momentum dissipation on tidal flats: A perturbation analysis. *Ocean Dynamics*, *68*(4–5), 439–455. https://doi.org/10.1007/s10236-018-1142-z

Huang, G., Falconer, R., Lin, B., & Xu, C. (2022). Dynamic tracing of fecal bacteria processes from a river basin to an estuary using a 2D/3D model. *River*, *1*(2), 149–161. https://doi.org/10.1002/rvr2.27

Hunt, S., Bryan, K. R., & Mullarney, J. C. (2015). The influence of wind and waves on the existence of stable intertidal morphology in meso-tidal estuaries. *Geomorphology*, *228*, 158–174. https://doi.org/10.1016/j.geomorph.2014.09.001

Jay, D. A. (1991). Green's law revisited: Tidal long-wave propagation in channels with strong topography. *Journal of Geophysical Research*, *96*(C11), 20585–20598. https://doi.org/10.1029/91JC01633

Kashefipour, S. M., Lin, B., Harris, E., & Falconer, R. A. (2002). Hydro-environmental modelling for bathing water compliance of an estuarine basin. *Water Research*, *36*(7), 1854–1868. https://doi.org/10.1016/S0043-1354(01)00396-7

Kim, B. G., & Cho, Y. K. (2017). Tide-induced residual circulation in a bay with laterally asymmetric depth. *Journal of Geophysical Research: Oceans*, *122*(5), 4040–4050. https://doi.org/10.1002/2016JC012473

Lee, H. J. (2010). Preliminary results on suspended sediment transport by tidal currents in Gomso Bay, Korea. *Ocean Science Journal*, *45*(3), 187–195. https://doi.org/10.1007/s12601-010-0017-0

Lerczak, J. A., & Geyer, W. R. (2004). Modeling the lateral circulation in straight, stratified estuaries*. *Journal of Physical Oceanography*, *34*(6), 1410–1428. https://doi.org/10.1175/1520-0485(2004)034<1410:MTLCIS>2.0.CO;2

Li, C., Schuttelaars, H. M., Roos, P. C., Damveld, J. H., Gong, W., & Hulscher, S. J. M. H. (2016). Influence of retention basins on tidal dynamics in estuaries: Application to the Ems Estuary. *Ocean & Coastal Management*, *134*, 216–225. https://doi.org/10.1016/j.ocecoaman.2016.10.010

Li, L., Guan, W., Hu, J., Cheng, P., & Wang, X. H. (2018). Responses of water environment to tidal flat reduction in Xiangshan Bay: Part I hydrodynamics. *Estuarine, Coastal and Shelf Science*, *206*, 14–26. https://doi.org/10.1016/j.ecss.2017.11.003

Li, L., Wang, X. H., Williams, D., Sidhu, H., & Song, D. (2012). Numerical study of the effects of mangrove areas and tidal flats on tides: A case study of Darwin Harbour, Australia. *Journal of Geophysical Research*, *117*(C6), C06011. https://doi.org/10.1029/2011JC007494

Li, X., Plater, A., & Leonardi, N. (2018). Modelling the transport and export of sediments in macrotidal estuaries with eroding salt marsh. *Estuaries and Coasts*, *41*(6), 1551–1564. https://doi.org/10.1007/s12237-018-0371-1

Ludwick, J. C. (1975). Variations in the boundary-drag coefficient in the tidal entrance to Chesapeake Bay, Virginia. *Marine Geology*, *19*(1), 19–28. https://doi.org/10.1016/0025-3227(75)90003-1

Luo, J., Ming, L., Sun, Z., & O'Connor, B. A. (2013). Numerical modelling of hydrodynamics and sand transport in the tide-dominated coastal-to-estuarine region. *Marine Geology*, *342*, 14–27. https://doi.org/10.1016/j.margeo.2013.06.004

Möller, I., Kudella, M., Rupprecht, F., Spencer, T., Paul, M., van Wesenbeeck, B. K., et al. (2014). Wave attenuation over coastal salt marshes under storm surge conditions. *Nature Geoscience*, *7*(10), 727–731. https://doi.org/10.1038/ngeo2251

Moore, R. D., Wolf, J., Souza, A. J., & Flint, S. S. (2009). Morphological evolution of the Dee Estuary, Eastern Irish Sea, UK: A tidal asymmetry approach. *Geomorphology*, *103*(4), 588–596. https://doi.org/10.1016/j.geomorph.2008.08.003

Murray, N. J., Phinn, S. R., Dewitt, M., Ferrari, R., Johnston, R., Lyons, M. B., et al. (2019). The global distribution and trajectory of tidal flats. *Nature*, *565*(7738), 222–225. https://doi.org/10.1038/s41586-018-0805-8

Namin, M., Lin, B., & Falconer, R. A. (2004). Modelling estuarine and coastal flows using an unstructured triangular finite volume algorithm. *Advances in Water Resources*, *27*(12), 1179–1197. https://doi.org/10.1016/j.advwatres.2004.08.012

Oey, L., Ezer, T., Hu, C., & Muller-Karger, F. E. (2007). Baroclinic tidal flows and inundation processes in Cook Inlet, Alaska: Numerical modeling and satellite observations. *Ocean Dynamics*, *57*(3), 205–221. https://doi.org/10.1007/s10236-007-0103-8

Restemeyer, B., Van Den Brink, M., & Woltjer, J. (2019). Decentralized implementation of flood resilience measures—A blessing or a curse? Lessons from the Thames Estuary 2100 Plan and the Royal Docks regeneration. *Planning Practice and Research*, *34*(1), 62–83. https://doi.org/10.1080/02697459.2018.1546918

Stark, J., Smolders, S., Meire, P., & Temmerman, S. (2017). Impact of intertidal area characteristics on estuarine tidal hydrodynamics: A modelling study for the Scheldt Estuary. *Estuarine, Coastal and Shelf Science*, *198*, 138–155. https://doi.org/10.1016/j.ecss.2017.09.004

Talke, S. A., & Jay, D. A. (2020). Changing tides: The role of natural and anthropogenic factors. *Annual Review of Marine Science*, *12*(1), 121–151. https://doi.org/10.1146/annurev-marine-010419-010727

Townend, I., & Whitehead, P. (2003). A preliminary net sediment budget for the Humber Estuary. *Science of the Total Environment*, *314–316*, 755–767. https://doi.org/10.1016/s0048-9697(03)00082-2

van der Wal, D., Pye, K., & Neal, A. (2002). Long-term morphological change in the Ribble Estuary, Northwest England. *Marine Geology*, *189*(3–4), 249–266. https://doi.org/10.1016/S0025-3227(02)00476-0

van Prooijen, B. C., & Wang, Z. B. (2013). A 1D model for tides, waves and fine sediment in short tidal basins—Application to the Wadden Sea. *Ocean Dynamics*, *63*(11–12), 1233–1248. https://doi.org/10.1007/s10236-013-0648-7

Verney, R., Brun-Cottan, J., Lafite, R., Deloffre, J., & Taylor, J. A. (2006). Tidally-induced shear stress variability above intertidal mudflats. Case of the macrotidal Seine Estuary. *Estuaries and Coasts*, *29*(4), 653–664. https://doi.org/10.1007/BF02784290

Winterwerp, J. C., & Wang, Z. B. (2013). Man-induced regime shifts in small estuaries—I: Theory. *Ocean Dynamics*, *63*(11–12), 1279–1292. https://doi.org/10.1007/s10236-013-0662-9

Winterwerp, J. C., Wang, Z. B., van Braeckel, A., van Holland, G., & Kösters, F. (2013). Man-induced regime shifts in small estuaries—II: A comparison of rivers. *Ocean Dynamics*, *63*(11–12), 1293–1306. https://doi.org/10.1007/s10236-013-0663-8

Wood, R. G., Black, K. S., Jago, C. F., Black, K. S., Paterson, D. M., & Cramp, A. (1998). Measurements and preliminary modelling of current velocity over an intertidal mudflat. *Geological Society - Special Publications*, *139*(1), 167–175. https://doi.org/10.1144/GSL.SP.1998.139.01.13

Zheng, L., Chen, C., & Liu, H. (2003). A modeling study of the Satilla River Estuary, Georgia. I: Flooding-drying process and water exchange over the salt marsh-estuary-shelf complex. *Estuaries*, *26*(3), 651–669. https://doi.org/10.1007/BF02711977

Zhu, R., Zhang, W., & Wei, X. (2025a). Impact of intertidal habitats on hydrodynamics in tidally energetic, well-mixed estuaries. *Journal of Physical Oceanography*, *55*(8), 1155–1191. https://doi.org/10.1175/JPO-D-23-0172.1

Zhu, R., Zhang, W., & Wei, X. (2025b). Model code used in the study "Impact of Intertidal Areas on Tidal Propagation in Tidally Dominated Estuaries" [Software]. *Zenodo*. https://doi.org/10.5281/zenodo.17477388